

# Photonic Crystal Fiber Long-Period Gratings as a Fiber-Optic Sensing Platform for Applications in Structural Health Monitoring

S. KRISHNASWAMY, S. ZHENG and Y. ZHU

## ABSTRACT

In this work, we explore the possibility of using photonic crystal fibers (PCFs) as a fiber-optic sensing platform for structural health monitoring, based on long-period gratings (LPGs). Two types of PCF-LPG sensors are proposed for detection of structure corrosion and vibration, respectively.

We numerically and experimentally investigate the behaviors of modal transition in the PCF-LPG humidity sensor where the air channels in PCF cladding are azimuthally coated with two types of nanostructured polymers as primary and secondary coatings using the electrostatic self-assembly deposition process. The primary coating does not have an effect on PCF-LPG parameters such as grating resonance wavelengths and their intensities that can be used for sensing, but it increases the sensitivity to refractive index of chemical analytes in the air channels. The secondary coating is for selective absorption of analyte molecules of interest. These two coatings significantly modify the cladding mode distribution of PCF-LPG and enhance the evanescent wave interaction with the external environment, resulting in a high sensitive and selective chemical sensor. We demonstrate a fiber-optic humidity sensor with the proposed nanofilm-coated PCF-LPG for detection of corrosion in civil infrastructural health monitoring.

We also develop a compact and robust PCF Mach-Zehnder interferometer (MZI) that can be used as an accelerometer for measurements of vibration. To excite the core mode to couple out with cladding modes, two LPGs with identical transmission spectra are written in the PCF. The first LPG can couple a part of the core mode to selected cladding modes. After the two light beams travel at different speeds over a certain length of the core and cladding, the cladding modes will be recoupled back to the core when they meet the second LPG, thus creating interference between the core mode and cladding modes. The dynamic strain is interrogated by the PCF-MZI that is attached on a spring-mass system. The shift of interference fringe can be measured by a photodetector, and the transformed analog voltage signal is proportional to the acceleration of the sensor head. The accelerometer has a capability of temperature insensitivity; therefore, no thermal-compensation scheme is required. Experimental results indicate that the PCF-MZI accelerometer may be a good candidate for applications in civil engineering infrastructure.

Sridhar Krishnaswamy, Shijie Zheng, and Yinian Zhu; Center for Quality Engineering and Failure Prevention, Northwestern University, 2137 Tech Drive, Evanston, IL 60208, USA



## INTRODUCTION

Structural health monitoring (SHM) is a process of carrying out damage detection, assessment and remediation of engineering structures, and it includes the functionalities of sensing, intelligence, and actuation to record, analyze, localize, and predict damage the remaining lifetime of structures. As a part of the suite of sensors used for diagnostics, fiber-optic sensors have attracted considerable attention in long-term structural monitoring.

One of the most frequent causes of infrastructure deterioration is the corrosion of concrete, in which water causes damages to structures. The ingress of water acts as a transporting vehicle for aggressive agents, such as chloride and sulfate ions, that penetrate into the concrete by capillary force. Water is also a reaction medium in destructive chemical processes, causing the corrosion of the concrete steel rebar. In general, the concentration of water in ambient air, which is expressed by relative humidity (RH), has a significant effect in the process of concrete corrosion. Therefore, it is important to implement a sensing tool such as a humidity sensor that allows for the early detection of corrosion within reinforced concrete structures, s, [1]. Among the measuring devices utilized in SHM, another type of transducer – accelerometers -- play a critical role in nondestructive assessment of large civil infrastructure. Currently popular electric accelerometers, however, have inherent limitations of electromagnetic interference, and heavy cabling.. With the advantages of optical fibers such as immunity to electromagnetic interference, light weight, anti-corrosion, and cost effectiveness, fiber-optic sensing technology is now increasingly being used for applications to sense acceleration [2].

In this work, we present a fiber-optic sensing platform for detection of RH using long-period grating (LPGs) inscribed in an endless single-mode PCF and coating nanostructure film into air channels in a photonic crystal fiber (PCF) cladding with modal transition of the LPG. Furthermore, we explore and demonstrate an in-fiber PCF Mach-Zehnder interferometer (MZI) based accelerometer integrated by a pair of identical LPGs.

## NANOFILM-COATED PCF-LPG HUMIDITY SENSORS

Fiber-optic grating refractometers have been increasingly investigated for the interrogation of refraction index changes of gas or aqueous solution [3]. They offer specific advantages such as high sensitivity, immunity to electromagnetic interference, accessibility to harsh and hostile environment [4], small size, and cost-effectiveness, to name just a few. LPGs as optical fiber humidity sensors have been reported for the applications in structural concrete condition monitoring to determine moisture ingress. An LPG couples the fundamental core mode to several co-propagating cladding modes in a single-mode fiber, resulting in a sequence of attenuation resonances in the transmission spectrum [5]. The LPG is an intrinsic and passive device that can be induced by a periodic refractive index modulation in the fiber core with a typical period of a few hundred micrometers. The sensitivity of LPG to the change of external refractive index is attributed to the dependence of the resonance wavelength and intensity on the effective refractive indices of cladding modes, which enables the use of LPGs as refractive index sensors based on the change in resonance wavelength and/or attenuation of the LPG transmission bands.

A PCF consists of regularly spaced air channels running along the fiber cladding. The core of the PCF is formed through missing an air channel at the center of the fiber. PCFs can trap and guide light in the core along the fiber via total internal reflection at a shallow angle of incidence but will refract light at steep angles on the core-cladding boundary, as in the conventional optical fibers [6,7]. PCFs are particularly attractive for use as an evanescent field sensing platform since they are both a waveguide and an analyte transmission cell, allowing intimate interaction between the analyte and the evanescent field of the guided light. LPGs in PCFs have been exploited for physical and chemical sensors. We inscribe LPGs in PCF to facilitate core mode to cladding mode coupling for evanescent field sensing. To fully explore the potential of PCF-LPG chemical sensors with high sensitivity and selectivity, we use two types of polymers as the nanofilm materials to be coated into the air channels of the PCF cladding for coupled cladding mode transition. Those two nanofilms significantly modify the cladding mode distribution of PCF-LPG and enhance the evanescent wave interaction with the external environment, achieving a high sensitive and selective humidity fiber sensor.

### Sensing principle of interior nanofilm-coated PCF-LPG

We used the MODE Solutions method to numerically predict cladding modes that are likely to be coupled with the fundamental guided core mode. The basic criteria will be (1) high coupling coefficient, (2) large mode field overlap, and (3) minimum confinement loss for propagation in cladding. We conducted a simulation of a LPG on PCF, which has 5 rings of air-channel in cladding, with a grating periodicity of 670  $\mu\text{m}$  and grating length of 14 periods ( $\sim 0.94$  cm). The analysis was specifically performed on  $LP_{04}$  cladding mode coupling with  $LP_{01}$  core mode of the LPG in the PCF. Shown in Fig. 1(a), (b), (c), and (d) are calculated power distribution in amplitude and phase of  $LP_{04}$  in the hexagonal region of two orthogonal degeneracy birefringence of  $E_X$  and  $E_Y$ , respectively. The PCF-LPG exhibits a resonance of -23 dB at wavelength 1550 nm and a confinement loss of 2.4 dB/cm. The analysis indicates that, for a given cladding symmetry, air-channel size, and channel-to-channel separation, confinement loss of  $LP_{04}$  cladding mode decreases exponentially with the increase of air-channel ring number, which is also a function of geometrical cladding microstructure.

Illustrated in Fig. 2 is the schematic for core-to-cladding mode coupling in a PCF-LPG structure, the working principle of which is based on the coupled-mode theory and the phase-matching condition. The resonance intensity corresponds to the amount of power transferred to the coupled cladding mode at the resonance wavelength.

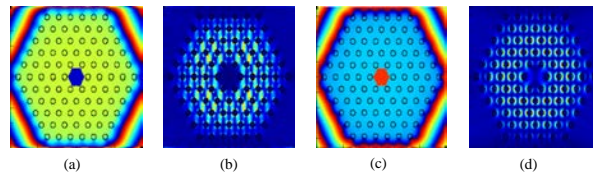


Figure 1. Simulated power distributions of  $LP_{04}$  cladding mode in the PCF excited by a LPG: (a)  $E_X$  in amplitude, (b)  $E_X$  in phase, (c)  $E_Y$  in amplitude, and (d)  $E_Y$  in phase.

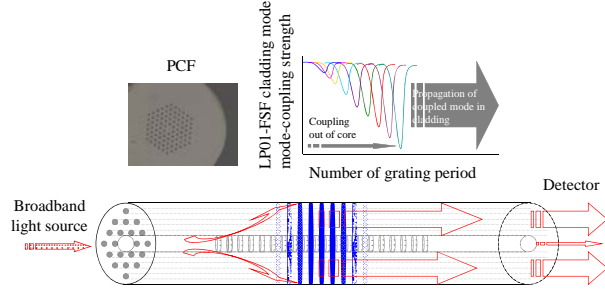


Figure 2. Schematic of core-to-cladding mode coupling in a PCF-LPG structure (top-left inset: the cross-sectional optical micrograph of PCF; top-right inset: dependence of mode coupling resonance on the grating design with the number of grating periods being an important parameter).

It is a function of the grating period number. The total power oscillating between the core mode and the coupled cladding mode is proportional to the minimum transmission. As seen in Fig. 1, for the simulated LPG in the PCF, the power distribution of  $LP_{02}$  cladding mode is extended in the silica segment around all air channels in the cladding after it is coupled with the  $LP_{01}$  core mode. The forward propagating  $LP_{02}$  cladding mode is very appealing for evanescent field interactions in the air cladding of the PCF.

Improvement of sensitivity and selectivity of the PCF-LPG sensors is a critical challenge in the field of the detection of chemical analytes. To this end, we coated two types of nanostructure polymer films, in which refractive index of the first nanofilm ( $PAH^+/PAA^-$ ) is higher than that of silica and refractive index of the second nanofilm ( $Al_2O_3^+/PSS^-$ ) is lower than that of silica, into the surfaces of air channels in the PCF-LPG. The new cladding mode is created and bonded within the first nanofilm that determines the change in the power distribution of cladding modes and their effective refractive indices. Because of the mode transition, the most part of light intensity of the lowest order of cladding mode moves to the first nanofilm, in which the evanescent field is drastically enhanced and the effective refractive index of the cladding mode is increased. As a result, the sensitivity of the PCF-LPG can be improved in terms of resonance wavelength shift and transmission intensity in response to change of external refractive index. The second nanofilm is able to interact specifically with water molecules by absorption, and it exhibits high selectivity.

### Nanofilm deposition in air-channels of PCF-LPG

To deposit the polymer nanofilms into the surface of air channels in the PCF-LPG cladding, we filled the air channels with polymer solution using layer-by-layer electrostatic self-assembly (ESA) deposition technique [8]. In order to know how long it takes for the polymer solution to pass through a given length of PCF-LPG, we used a capillary filling model to numerically calculate the dependence of time on length of PCF with a given geometry under different pressures. Shown in Fig. 3 is the schematic diagram of capillary tube with liquid inside and contact angle between the rim of the liquid and the wall of capillary. The capillary force can push the liquid out of the capillary when the contact angle is larger than  $90^\circ$ , as seen in Fig. 3(a), while the capillary force can pull the liquid into the capillary when the contact angle is smaller than  $90^\circ$  as seen in Fig. 3(b).

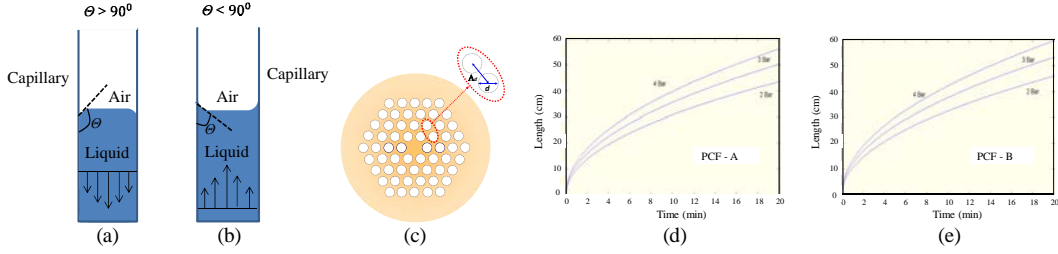


Figure 3. (a) The liquid is pushed out of the capillary by capillary force with contact angle larger than  $90^\circ$ , (b) the liquid is pulled into the capillary by capillary force with contact angle smaller than  $90^\circ$ , (c) schematic of a cross-sectional PCF with 4 rings of air-channel in cladding (d: diameter of air-channel and  $\Lambda_d$ : distance of channel-to-channel separation), numerically calculated water filling time of air channels at pressure differences of 2-bar, 3-bar, and 4-bar for (d) PCF-A with  $d$  of  $3.76 \mu\text{m}$  and  $\Lambda_d$  of  $8.99 \mu\text{m}$  and (e) PCF-B with  $d$  of  $4.23 \mu\text{m}$  and  $\Lambda_d$  of  $8.07 \mu\text{m}$ .

Water/solution flow in air channels of PCF is induced by a constant positive pressure difference, resulting in a Poiseuille flow in the PCF channels [9]. For an air-channel PCF with diameter of  $d$ , length of  $l$ , water viscosity of  $\eta$ , and in the presence of a uniform pressure difference of  $\Delta p$ , the water flow rate can be expressed by:

$$Q = \frac{\pi d^4 \cdot \Delta p}{128 \eta l} \quad (1)$$

For example, at  $\Delta p$  of 5-bar, it takes only 1.2 minutes for water to fill in the air channels with  $d$  of  $4 \mu\text{m}$  and  $l$  of 1-meter PCF. We have numerically calculated the water filling time of PCF air channels with the pressure differences of 2-bar, 3-bar, and 4-bar. Two types of PCF geometrical parameters were used with  $d$  of  $3.76 \mu\text{m}$  and  $\Lambda_d$  (distance of channel-to-channel separation) of  $8.99 \mu\text{m}$  in PCF-A and  $d$  of  $4.23 \mu\text{m}$  and  $\Lambda_d$  of  $8.07 \mu\text{m}$  in PCF-B. Shown in Fig. 3(c) is the diagram of a cross-sectional PCF with 4 rings of air-channel in cladding. From Fig. 3(d) and (e), it can be clearly seen that, the larger the diameter of air channel, the longer the filling length at the same filling time, which is also experimentally confirmed.

## Experimental results and discussion

To accelerate the liquid flow speed, we pressurize one end of the PCF while the other end of the fiber is immersed in water. Depicted in Fig. 4(a) is the schematic of compressed air pressure chamber that houses the flow entrance end of the PCF and a vial that contains water/solution. Fig. 4(b) shows a drop of water out of air channels of the PCF, the length of which is 60 cm. Two PCFs (PCF (1) and PCF (2)) with different geometrical parameters are used for pressurized water filling experiments. PCF (1) has  $d$  of  $3.76 \mu\text{m}$ ,  $\Lambda_d$  of  $7.03 \mu\text{m}$ , and core diameter of  $8.99 \mu\text{m}$ , while PCF (2) has  $d$  of  $4.23 \mu\text{m}$ ,  $\Lambda_d$  of  $8.07 \mu\text{m}$ , and core diameter of  $11.94 \mu\text{m}$ . SEM images of cross-sections of PCF (1) and PCF (2) are shown in the insets of Fig. 4(c) and (d), respectively, shown in which are the respective dependences of pressurized water filling time on filling lengths of PCF (1) and PCF (2) under pressures of 2-bar, 3-bar, and 4-bar. It can be seen that, at pressure of 2-bar, it takes longer time for PCF (2) than PCF (1) to fill water into air channels with the same length because viscous friction force dominates the entire flow mechanism. Meanwhile, there is no clear difference of the filling length below 5 minutes with pressures of 2-bar, 3-bar, and 4-bar in PCF (1). At higher pressure, much less filling

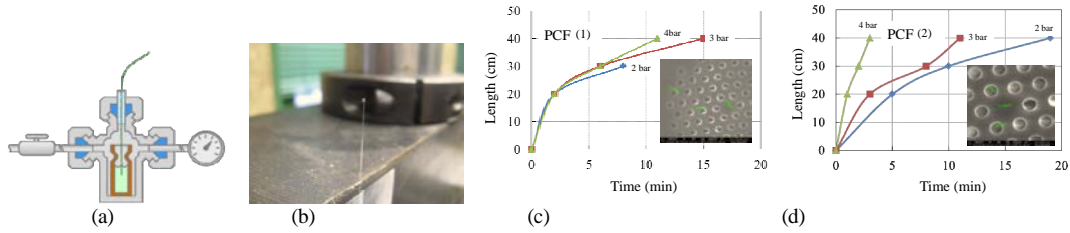


Figure 4. (a) Schematic of compressed air pressure chamber for the filling of water/polymer solution, (b) a picture showing a drop of water out of air channels of the PCF-LPG, dependence of pressurized water filling time on length with different pressure for (c) PCF(1) with  $d$  of  $3.76 \mu\text{m}$ ,  $A_d$  of  $7.03 \mu\text{m}$  and core diameter of  $8.99 \mu\text{m}$  (inset: SEM image of this fiber cross-section), and (d) PCF(2) with  $d$  of  $4.23 \mu\text{m}$ ,  $A_d$  of  $8.07 \mu\text{m}$ , and core diameter of  $11.94 \mu\text{m}$  (inset: SEM image of this fiber cross-section).

time is needed in PCF (2) than in PCF (1) for filling water into a given length of air channels. For example, it takes 3 minutes and 11 minutes to fill water into a length of 40-cm PCF (2) under pressures of 4-bar and 3-bar, respectively, but under the same pressures it takes about 11 minutes and 15 minutes, respectively, to fill the same length of PCF (1). In this aspect, we will use 4-bar or higher pressure for filling of polymer solutions in the experiments.

To coat the nanofilms on the exterior fiber surface by the ESA technique, the PCF needs to be exposed to cationic and anionic solutions. More details about nanofilms deposited on the exterior surface of PCF-LPG can be found in the Ref. [10]. Since the nanofilms are to be created in the interior surface of PCF air channels, a compressed air pressure chamber was used to pressurize the polymer solution through the air channels. A 60-cm long PCF-LPG was inserted into the chamber where there is the vial containing Milli-Q water for washing the surface of air channels. After cleaning, the surface of the air channels was negatively charged. The Milli-Q water in the chamber was removed and replaced by positively-charged  $\text{PAH}^+$  solution. After seeing a drop of the solution at the end of the PCF-LPG and waiting for 3 minutes, we removed the fiber from the chamber, and replaced Milli-Q water in order to wash the excess of  $\text{PAH}^+$  polymer molecules. Then a negatively-charged  $\text{PAA}^-$  solution was into the air channels, and the same deposition procedure was repeated. The consecutive layers of positively- and negatively-charged polymers are called for bi-layer. Several bi-layers of  $\text{PAH}^+/\text{PAA}^-$  were deposited first for the primary coating. Then, another type of bi-layer of  $\text{Al}_2\text{O}_3^+/\text{PSS}^-$  was deposited with several times on the bi-layers of  $\text{PAH}^+/\text{PAA}^-$  as the secondary coating. Shown in Fig. 5 are the SEM images for (a) cross-section of interior nanofilm-coated PCF-LPG with  $\text{PAH}^+$  and  $\text{PAA}^-$ , in which some air channels are blocked due to the residue of  $\text{PAH}^+/\text{PAA}^-$  polymerization; (b) thickness of 3 bi-layers of  $\text{PAH}^+$  and  $\text{PAA}^-$  ( $48.3 \text{ nm}$ ); (c) cross-section of interior nanofilm-coated PCF-LPG with  $\text{Al}_2\text{O}_3^+$  and  $\text{PSS}^-$ ; and (d) thickness

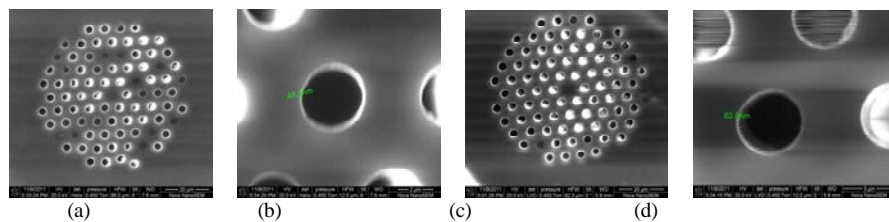


Figure 5. SEM images for (a) cross-section of interior nanofilm-coated PCF-LPG with  $\text{PAH}^+$  and  $\text{PAA}^-$ , (b) thickness of 3 bi-layers of  $\text{PAH}^+$  and  $\text{PAA}^-$ , (c) cross-section of interior nanofilm-coated PCF-LPG with  $\text{Al}_2\text{O}_3^+$  and  $\text{PSS}^-$ , and (d) thickness of 5 bi-layers of  $\text{Al}_2\text{O}_3^+$  and  $\text{PSS}^-$ .

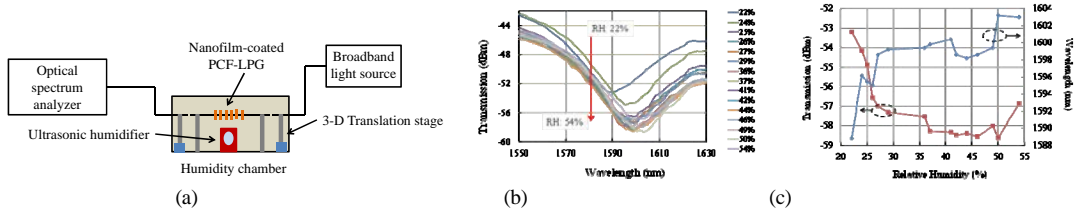


Figure 6. (a) Experimental setup for testing of the interior nanofilm-coated PCF-LPG response to humidity, (b) evolution of transmission spectra of the interior nanofilm-coated PCF-LPG for various RH from 22% to 54%, and (c) dependences of grating resonance wavelength and intensity on RH.

of 5 bi-layers of  $\text{Al}_2\text{O}_3^+$  and  $\text{PSS}^-$  (82.0 nm). A slightly roughness of the nanofilms is because of the formation of polymer chain. The thickness of the nanofilm can be precisely controlled by the number of the deposited bi-layer, while the polymetric materials of nanofilms are determined by the chemical detection that is based on the change of a property of the sensing material as a consequence of sorption and desorption of a specific analyte. The properties of the nanofilms make themselves not only sensitive but also selective to water molecules.

The experimental setup used for testing of interior nanofilm-coated PCF-LPG response to humidity is shown in Fig. 6(a). A broadband superluminescent light-emitting diode (SLED) light source is connected to a single-mode fiber that is fixed on a 3-D translation stage with a fiber clumper. The single-mode fiber is butt-connected to one end of the interior nanofilm-coated PCF-LPG, the other end of which is also butt-connected to another single-mode fiber that is fixed with a fiber clumper on another 3-D translation stage, too, and goes to an OSA. In this way, the moisture can be diffused through the air channels of the interior nanofilm-coated PCF-LPG. Meantime, an optically aligned (within  $\pm 1\mu\text{m}$ ) single-mode light can be propagated into and out of the interior nanofilm-coated PCF-LPG for signal collection. A home-made humidity chamber houses all of the 3-D translation stages, the interior nanofilm-coated PCF-LPG, a mini ultrasonic humidifier that consists of a digital temperature and the humidity meter. The responses of interior nanofilm-coated PCF-LPG to changing of RH at room temperature ( $24.5^\circ\text{C}$ ) have been tested. Shown in Fig. 6(b) are the transmission spectra of interior nanofilm-coated PCF-LPG with different RH level, while Fig. 6(c) is the dependences of resonance intensity and wavelength on RH. As the RH increase from 22% to 54%, the more water molecules are adsorbed on the nanofilm, the stronger the light absorption from transited cladding mode is. The transmission power of resonance dip is getting significantly low, as brown line shown in Fig. 6(c). On the other hand, when the secondary nanocoating absorbs more water molecules with the increase of RH, the effective refractive index of cladding increases, leading to a significant shift of resonance wavelength towards “blue” side, which is indicated in blue line shown in Fig. 6(c). The average coefficients of RH-wavelength and RH-intensity are  $0.0019\%/ \text{pm}$  and  $0.0051\%/10^{-3}\text{dBm}$ , respectively, which are more sensitive than other LPG humidity sensors reported in the literature.

## TEMPERATURE INSENSITIVE PCF-MZI ACCELEROMETERS

The implementation of fiber Bragg grating (FBG)-based sensors in structural health monitoring and civil engineering is increasing sharply in recent years. However, the FBG accelerometers developed so far have shortcomings such as poor sensitivity, temperature dependence, and nonlinear behavior [11-13]. For a

practical point of view, vibration-based structural health monitoring requires that an accelerometer possesses high sensitivity to acceleration-induced strain and low sensitivity to temperature. The sensitivity of FBGs to strain and temperature are  $\sim 1.2 \text{ pm}/\mu\epsilon$  and  $\sim 10 \text{ pm}/^\circ\text{C}$  [14], indicating that a temperature-compensation scheme has to be considered for a FBG accelerometer. The conventional way of temperature-compensation is to install an additional independent temperature sensor and then to subtract the temperature-induced strain by calibration, adding to the complexity of the system. Integrated PCF-MZI accelerometers, which we present in this paper, do not require a temperature-compensation scheme and have the potential of becoming a critical enabler for fiber-optic based portable vibration probes.

### Numerical analysis of coupled cladding modes in a PCF-MZI

The MZI is a particularly simple device for demonstrating of interference by division of amplitude. A light beam is first split into two parts by a beam splitter and then recombined by a second beam splitter, and sent to a photodetector to be analyzed. The optical path lengths in the two arms are either nearly identical or different with an extra delay line. If the two optical path lengths are different, there will be some interference fringe patterns in both outputs.

The PCF-MZI can easily be constructed in the following way: inscription of two identical LPGs with a separation length of  $L$  in a PCF. Shown in Fig. 7(a) is a schematic of PCF-MZI. The basic principle of PCF-MZI is the same as that of free space MZI. The first LPG acts to couple light to a cladding mode. Light then propagates to the second LPG via two routes, namely in the core and in the cladding. At the second LPG, the cladding mode is coupled back into the core. In an index-guiding PCF, a cladding mode has a smaller effective refractive index than that of the core mode. Since the physical lengths of two PCF-MZI arms are exactly the same, the spatial frequency of the wavelength spectrum is directly related with the difference of effective refractive indices between the core mode and the coupled cladding mode. By virtue of the difference between the effective refractive indices of the core and cladding modes, the light coupled into the core by the second LPG is phase shifted with respect to the light that propagates through the core, giving rise to the interference fringe pattern. The interference transmission power intensity of the PCF-MZI can be expressed as a function of the core mode intensity  $I_{core}(\lambda)$ , the cladding mode intensity  $I_{clad}(\lambda)$ , and the phase difference  $\Delta\varphi$  accumulated during a physical length  $L$ :

$$T(\lambda) = I_{core}(\lambda) + I_{clad}(\lambda) + 2[I_{core}(\lambda)I_{clad}(\lambda)]^{1/2}\cos \Delta\varphi \quad (2)$$

where  $\Delta\varphi = 2 \cdot \pi \cdot L \cdot \Delta n_{eff}/\lambda$ ,  $\Delta n_{eff} = n_{core}^{eff} - n_{clad(i)}^{eff}$  in which  $n_{core}^{eff}$  and  $n_{clad(i)}^{eff}$  are the effective refractive indices of the core and the  $i^{th}$  order cladding mode. Since the LPG interval length in PCF should not be too long for a compact sensor, the performance improvement of such a pair of LPG relies on the cladding mode with low confinement loss to be coupled in cladding then to be coupled back to core. To this end, we have performed numerical calculations of the confinement loss of coupled cladding mode in a PCF-MZI.

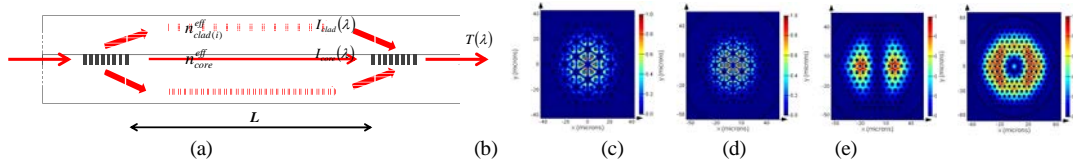


Figure 7. Schematic of PCF-MZI ( $L$ : separation length between two identical LPGs), the lowest order of cladding modes that are most likely coupled by LPGs in a PCF ( $d$ :  $2.8 \mu\text{m}$  and  $A_d$   $7 \mu\text{m}$ ) with variety layers of air-channel rings calculated at wavelength of  $1550 \text{ nm}$  for (b) 5 layers with mode radius of  $35.15 \mu\text{m}$  and confinement loss of  $75.05 \text{ dB/m}$ , (c) 6 layers with mode radius of  $40.4 \mu\text{m}$  and confinement loss of  $48.02 \text{ dB/m}$ , (d) 7 layers with mode radius of  $45.6 \mu\text{m}$  and confinement loss of  $14.37 \text{ dB/m}$ , and (e) 8 layers with mode radius of  $50.82 \mu\text{m}$  and confinement loss of  $1.87 \text{ dB/m}$ .

The numerical analysis of index-guiding PCFs has indicated that, for an optimized hexagonally patterned air-channel in cladding with  $d$  of  $\sim 2.8 \mu\text{m}$  and  $A_d$  of  $\sim 7 \mu\text{m}$ , the confinement loss of the most likely coupled cladding mode by a LPG decreases exponentially with the increase of layers of the air-channel rings, which is illustrated in Fig 7(b)-(e). The results of the numerical calculations also reveal that for 8 layers of hexagonally patterned air-channel ring of PCF the confinement loss is an acceptable  $1.87 \text{ dB/m}$ .

## Fabrication of PCF-MZI

The air-channel structure in the cladding of an index-guiding PCF determines the optical properties of the fiber, which provides a large degree of freedom in tailoring the characterization of the cladding modes through control of the geometries of air-silica cladding. The optimal PCF-MZI configuration and characterization can be realized using a  $\text{CO}_2$  laser inscription of a pair of LPGs in the PCF. Fig. 8(a) depicts a system for the laser inscription process. A  $\text{CO}_2$  laser is aided with a galvanometer-based 1-D scanning head that directs the laser beam to the PCF following precisely a prescribed path with predetermined parameters such as exposure time, energy, number of periods. The transmission characteristics of the PCF-MZI is monitored *in situ* during the inscription process with the PCF coupled to a SLED broadband light source at one end and an optical spectrum analyzer (OSA) at the other end. Shown in Fig. 8(b) is an experimental setup of  $\text{CO}_2$  laser system by which the LPGs are inscribed in the PCFs with residual stress relaxation technique and point-by-point method. The *in situ* capability allows real-time monitoring of the evolution of the two beam interference as the number of periods of the second LPG increase.

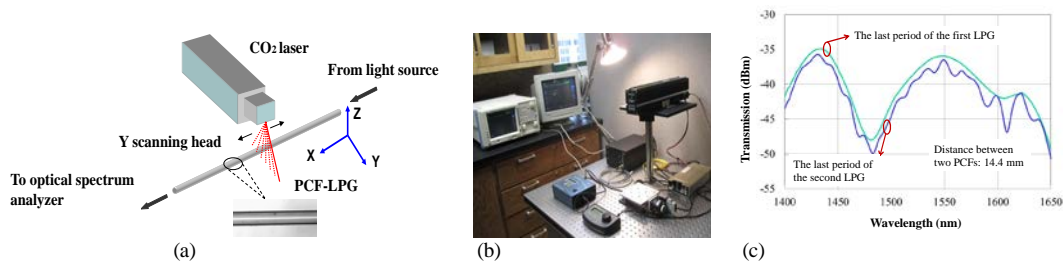


Figure 8. Schematic of experimental setup for PCF-LPG fabrication by  $\text{CO}_2$  laser (inset: SEM image of  $\text{CO}_2$  laser induced PCF-LPG), (b) a photo showing the setup that includes SLED broadband light source, OSA,  $\text{CO}_2$  laser with 1-D scanning head, and 2-D micro-translation stage with fiber holders, and (c) transmission spectra of the PCF-MZI with the last periods of the first and the second LPGs.

The proposed PCF-MZI has its own transmission spectrum that exhibits a series of interference fringe with period of maxima and minima given by  $\lambda^2/(\Delta n_{eff} L)$ . The maxima appear when  $2\pi\Delta n_{eff}L/\lambda = 2m\pi$ , being  $m = 1, 2, 3, \dots$ . This means at wavelength given by

$$\lambda_m = \Delta n_{eff}L/m \quad (3)$$

By differentiating Eq. (3) with respect to temperature, the shift of the  $n^{th}$  interference peak can be obtained, that is  $\Delta\lambda_n = (\alpha + p_t)\lambda_m\Delta T$ , where  $\alpha = (1/L)\partial L/\partial T$  is the thermal change of length whose value is  $\sim 5 \times 10^{-7}/^\circ\text{C}$  for pure silica;  $p_t = (1/\Delta n_{eff})\partial(\Delta n_{eff})/\partial T$  is the contribution to the thermal change of difference between the mode indices of core and cladding in the PCF-MZI, and  $\Delta T$  is the temperature change. Since two coupled modes are in the same dopant-free waveguide, therefore, a  $\Delta T$  must affect the two modes in a similar manner, and as a result the sensor is temperature insensitive. It has been reported that the temperature sensitivity of PCF-MZI was found to be  $\sim 3 \text{ pm}/^\circ\text{C}$  at wavelength of 1550 nm [15]. It has also been reported that the strain sensitivity of PCF-MZI is  $\sim -3 \text{ pm}/\mu\epsilon$  at wavelength of 1550 nm, which is much higher than FBG-based strain sensors ( $\sim 1.2 \text{ pm}/\mu\epsilon$ ) [16]. The two identical LPGs in the PCF for the core mode coupling out with cladding mode and then cladding mode coupling back into core is also subject to temperature, although the sensitivity of two PCF-LPGs are very low, but they have the same temperature factor to ensure that during the homogenous temperature change both LPGs shift the resonance wavelengths in the same way, so that the coupling process is always self-referenced. Owing to the high strain sensitivity and very low thermal sensitivity of PCF-MZI, the temperature compensation would be not necessary for the PCF-MZI sensors that are operated in a normal temperature environment. Fig. 8 (c) shows the evolution transmission spectra of the PCF-MZI with the distance of 14.4 mm between the last period of the first LPG and the last period of the second identical LPG.

### Design and assembly of PCF-MZI sensing head of accelerometer

Typical desirable features for the sensor head of an accelerometer designed for field applications include low noise (about  $1 \text{ mg}/\text{Hz}^{1/2}$  at a few hertz for structural grade sensing), minimal cross-axis sensitivity (less than 25 dB below axial responsivity), small size and weight, immunity from all physical measurands except for strain, and an ability to be multiplexed for multipoint sensing. We have designed and assembled a sensor head for accelerometer by using a PCF-MZI as a transducer which allows for the demonstration of a fully packaged PCF-MZI

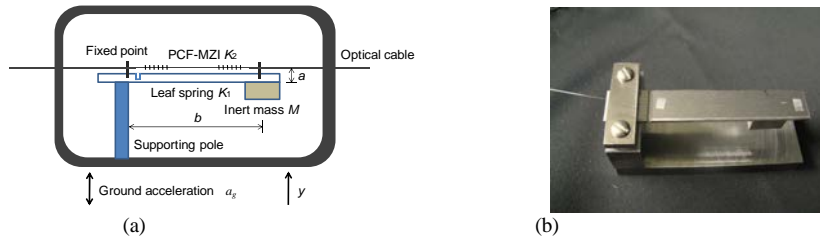


Figure 9. (a) Schematic of the PCF-MZI sensor head of mechanical part design for accelerometer and (b) experimental setup of the PCF-MZI sensor head of the accelerometer.

accelerometer that has numerous desirable engineering features, including both temperature and cross-axis insensitivity, as well as the correlation of resonant frequency, sensitivity, and material parameters.

Shown in Fig. 9(a) is a schematic of the PCF-MZI sensor head of the accelerometer. The two ends of the PCF-MZI sensor are fixed directly on the leaf spring of a spring-mass configuration. In the system design, the PCF-MZI is not directly bonded to the cantilever, avoiding possible non-uniform strain in the PCF-MZI. Instead, the PCF-MZI is uniformly tensioned, achieving a constant strain distribution over the PCF-MZI. By employing this configuration, the PCF-MZI is always subject to uniform strain profile along its measuring length, resulting in a sharp interferometric fringe with no broadening in its spectrum. The cantilever spring is used here to minimize cross-axis sensitivity. An inert mass made of brass is attached to one end of the spring made of stainless steel. The other end of the cantilever spring is supported by a supporting pole. This pole is fixed on the base of sensor enclosure and the whole sensor head is fully coupled into the testing object with only the optical fiber cable stretching out. Fig. 9(b) shows the prototype of the PCF-MZI accelerometer.

Vibration from  $y$  direction in Fig. 9(a) can induce the ground acceleration ( $a_g$ ) change on the sensor enclosure together with the supporting pole at one end of the leaf spring ( $K_1$ , stiffness of leaf spring). While the inert mass ( $M$ ) hanging at the other end of the leaf spring remains relatively static, it induces a strain variation on the spring together with the PCF-MZI sensor head. The strain change of the PCF-MZI can be detected by the shift of interferometric fringe according to the sensing principle. The mechanical system of the sensor head can be modeled as a single-degree-of-freedom system. The PCF-MZI can be simplified as a fiber spring ( $K_2$ , stiffness of fiber spring). The equation of motion for the system can be expressed as:

$$M \frac{\partial^2 y}{\partial t^2} + \left[ K_1 + \left( \frac{a}{b} \right)^2 K_2 \right] y = -M a_g \quad (4)$$

where  $\frac{\partial^2 y}{\partial t^2}$  is the ground acceleration. Motion is along  $y$  axis. The dimension  $a$  is the distance from the fiber to the bottom of the leaf spring, while the dimension  $b$  is the distance between two fixed points. The natural frequency  $f_0$  can be defined as:

$$f_0 = \frac{1}{2\pi} \sqrt{\left[ K_1 + \left( \frac{a}{b} \right)^2 K_2 \right] / M} \quad (5)$$

and the fiber spring can be given by:  $K_2 = E \cdot A / b$ , where the elastic modulus of silica of  $E$  is  $7.3 \times 10^{10}$  M/m<sup>2</sup>, and  $A$  is the cross-sectional area of the fiber. The fiber diameter is typically 125  $\mu$ m. Strain induced by acceleration in PCF-MZI is expressed by:  $\varepsilon \approx -k \cdot A_g$  where  $A_g$  is the acceleration amplitude and  $k = a / [b^2 \cdot (2\pi f_0)^2]$  is the sensitivity coefficient of the PCF-MZI accelerometer. We can see that the natural frequency is determined by five parameters  $a$ ,  $b$ ,  $K_1$ ,  $K_2$ , and  $M$ . It increases with increase of  $K_1$ ,  $K_2$ ,  $a$ , and decrease of  $b$  and  $M$ . By adjusting the parameters of  $a$ ,  $b$ ,  $M$  and choosing material  $K_1$ , the system can be customized as the frequency response sensor.

## Testing results and discussions

To verify the performance of the PCF-MZI sensor head as an accelerometer, a dynamic testing was carried out in the laboratory environment. Shown in Fig. 10 (a) is a diagram of the interrogation scheme for PCF-MZI sensor head. A 1550 nm narrow band laser source (center wavelength around 1550 nm, and optical output power of ~ 25 mW) is launched into a single-mode fiber (SMF) and then enters the PCF-MZI sensor head. The output from the PCF-MZI sensor head that is mounted on a vibration table (vibration frequency can be adjusted) goes to the photodetector, where the optical signal is converted into analog electrical signal which is finally collected and plotted in the computer and monitored by an oscilloscope *in situ*. Shown in inset of Fig. 10 (a) is the experimental setup of the PCF-MZI accelerometer.

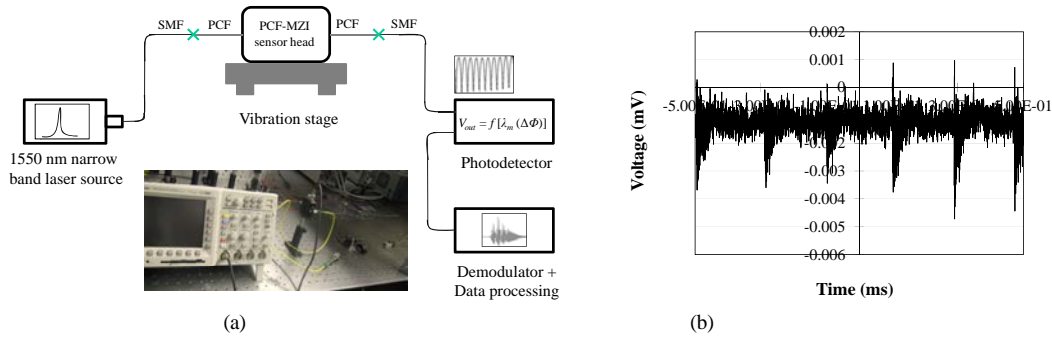


Figure 10. (a) Diagram of interrogation scheme of the PCF-MZI accelerometer (inset: the experimental setup of the PCF-MZI accelerometer) and (b) oscilloscope signal by vibrating the cantilever in the PCF-MZI sensor head.

We mounted the PCF-MZI accelerometer on an optical table for a vibration testing and qualitatively tested the PCF-MZI accelerometer by pressing and vibrating the cantilever in the PCF-MZI sensor head. Fig. 10 (b) shows the testing results of the PCF-MZI accelerometer measured by oscilloscope, indicating that the input vibrating frequency is about 5 kHz. The damping of the PCF-MZI accelerometer is a key factor to determine its acceleration sensitivity and dynamic range. A high damping will sacrifice the low frequency response while lower damping will result in the improper oscillation time of the spring. The sensor detection dynamic range is estimated by the values of maximum output and background noise. Further experiments will be conducted on how to improve the sensitivity of the PCF-MZI accelerometer.

## CONCLUSION

In conclusion, we have presented an interior nanofilm-coated PCF-LPG with high sensitivity and selectivity for humidity detection by depositing PAH<sup>+</sup>/PAA<sup>-</sup> and Al<sub>2</sub>O<sub>3</sub><sup>+</sup>/PSS<sup>-</sup> with layer-by-layer ESA technique on the surface of air channels in a PCF-LPG. Experimental results indicate that the resonance intensity has decreased significantly with increase of RH while the resonance wavelength drastically shifts toward “blue” side, compared to the types of LPG humidity sensors. The developed interior nanofilm-coated PCF-LPG sensors are useful for detection of corrosion in civil infrastructural health monitoring.

We have also developed a PCF-MZI based accelerometer by integrating a pair of LPGs in PCF for real-time detection of strain variation caused by vibration. The performance of the PCF-MZI transducer has been experimentally investigated, and the sensitivity of the PCF-MZI accelerometer is comparable to FBG-based counterparts. The advantages of the PCF-MZI accelerometer include immunity to electromagnetic interference, capability to transmit signals over long distance without any additional amplifiers, high sensitivity of fringe shift to strain, and temperature insensitivity.

## ACKNOWLEDGMENT

This research work has partially been supported by a US National Science Foundation PIRE-ISHM with award OISE-0730259 as well as by the US Department of Transportation through the Infrastructure Technology Institute at Northwestern University.

## REFERENCES

1. T. Venugopalan, T. Sun, K. T. V. Grattan, "Long-period grating-based humidity sensor for potential structural health monitoring," *Sens. Actuators A* 148(1), 57-62 (2008).
2. M. D. Todd, J. M. Nichols, S. T. Trickey, M. Seaver, C. J. Nichols, and L. N. Virgin, "Bragg grating-based fiber optic sensors in structural health monitoring," *Phil. Trans. R. Soc. A* 365(12), 317-343 (2007).
3. M. P. Delisa, Z. Zhang, M. Shiloach, S. Pilevar, C. C. Davis, J. S. Sirks, and W. E. Bentley, "Evanescent wave long-period fiber Bragg grating as an immobilized antibody biosensor," *Anal. Chem.* 72(13), 2895-2900 (2000).
4. T. Wei, J. Montoya, J. Zhang, J. Dong, and H. Xiao, "Fabrication of long-period fiber gratings by CO<sub>2</sub> laser irradiations for high temperature applications," *Proc. SPIE* 6757, 675708 (2007).
5. T. Erdogan, "Fiber grating spectra," *J. Lightwave Technol.* 15(8) 1277-1294 (1997).
6. P. St. J. Russell, "Photonic crystal fibers," *Science* 299(5605), 358-362 (2003).
7. T. A. Birks, J. C. Knight, and P. St. J. Russell, "Endless single-mode photonic crystal fiber," *Opt. Lett.* 22(13), 961-963 (1997).
8. G. Decher, "Fuzzy nanoassemblies: toward layered polymeric multicomposites," *Science* 277(5330), 1232-1237 (1997).
9. J. Pfizner, "Poiseuille and his law," *Anaesthesia* 31(2), 273-275 (1976).
10. S. Zheng, Y. Zhu, and S. Krishnaswamy, "Nanofilm-coated long-period fiber grating humidity sensors for corrosion detection in structural health monitoring," *Proc. SPIE* 7983, 79831A-8 (2011).
11. A. D. Kersey, D. A. Jackson, and M. Corke, "High sensitivity fiber-optic accelerometer," *Electron. Lett.* 18, 559-561 (1982).
12. S. Vohra, B. Danver, A. Tveten, and A. Dandridge, "High performance fiber optic accelerometers," *Electron. Lett.* 33, 155-157 (1997).
13. T. A. Berkoff and A. D. Kersey, "Experimental demonstration of a fiber Bragg grating accelerometer," *IEEE Photon. Technol. Lett.* 8(12), 1677-1679 (1996).
14. A. D. Kersey, M. A. Davis, H. J. Patrick, M. LeBlanc, K. P. Koo, C. G. Askin, M. A. Putnam, and E. J. Friebele, "Fiber grating sensors," *J. Lightwave Technol.* 15(8), 1442-1463 (1997).
15. J. Villatoro, V. Finazzi, V. P. Minkovich, V. Prunèi, and G. Badenes, "Temperature-insensitive photonic crystal fiber interferometer for absolute strain sensing," *Appl. Phys. Lett.* 91, 091109 (2007).
16. W. Shin, Y. L. Lee, B.-A. Yu, Y.-C. Noh, and T. J. Ahn, "Highly sensitive strain and bending sensor based on in-time fiber Mach-Zehnder interferometer in solid core large mode area photonic crystal fiber," *Opt. Commun.* 283(10), 2097-2101 (2010).